Journal of Applied Mathematics and Physics, 2022, 10, 2026-2039
https://www.scirp.org/journal/jamp
ISSN Online: 2327-4379
ISSN Print: 2327-4352

Structural, Magnetic and Transport Properties of Gd and Cu Co-Doped $BiFeO_3$ Multiferroics

Sajal Chandra Mazumdar[1*], Sanjib Datta[1], Farhad Alam[2]

[1]Department of Physics, Comilla University, Cumilla, Bangladesh
[2]Department of Physical Sciences, Independent University, Bangladesh, Dhaka-1229, Bangladesh
Email: *sajalf@yahoo.com

How to cite this paper: Mazumdar, S.C., Datta, S. and Alam, F. (2022) Structural, Magnetic and Transport Properties of Gd and Cu Co-Doped $BiFeO_3$ Multiferroics. *Journal of Applied Mathematics and Physics*, **10**, 2026-2039.
https://doi.org/10.4236/jamp.2022.106138

Received: May 28, 2022
Accepted: June 27, 2022
Published: June 30, 2022

Abstract

The novel polycrystalline $Bi_{0.85}Gd_{0.15}Cu_xFe_{1-x}O_3$ (x = 0, 0.025, 0.05, 0.075, 0.10) multiferroics are synthesized by the usual solid-state reaction route. The synthesis of the desired phase has been verified by the X-ray Diffraction (XRD) patterns. With major structural phases, few traces of secondary phases of $Bi_2Fe_4O_9$ and $Bi_{25}FeO_{40}$ appear for all the compositions. A discontinuous series of structural changes with varying compositions are observed for the doped samples. The bulk density (ρ_B) increases with Cu content reaches the highest at x = 0.05 and then declines. The complex initial permeability and dielectric characterizations are performed by Wayne Kerr Impedance Analyzer. The x = 0.05 samples having maximum density exhibit the highest permeability (μ_i') implying a close relation between μ_i' and the density. The reduction of μ_i' at higher Cu concentration is due to the low density of the samples associated with the increased intragranular pores. The dielectric constant (ε') is measured against frequency in the range 1 kHz - 10 MHz. It is perceived that ε' falls with the rise in frequency up to 100 kHz. This dielectric dispersion is observed at a lower frequency as a result of interfacial polarization outlined by Maxwell-Wagner. The maximum ε' is obtained for x = 0.025 composition. In the low-frequency range, the AC conductivity σ_{AC} is practically independent of frequency and resembles the DC conductivity (σ_{DC}). In the vicinity of high frequency recognized as the hopping region, σ_{AC} rises since the conductive grains are more active at high frequencies. The co-doping with Gd and Cu in $BiFeO_3$ ceramics enhances the magnetic and dielectric properties of the ceramics and hence can be utilized for fabricating multifunctional devices.

Keywords

X-Ray Diffraction, Permeability, Dielectric Constant, Conductivity

1. Introduction

Multiferroic materials have lately achieved great attraction because of their versatile device applications and triggering new physics. Multiferroics combine various primary ferroic orders in a single phase [1]. Conventionally, multiferroics unite ferroelectricity and ferromagnetism or, more liberally, with every kind of magnetism [2]. The major attractive feature of multiferroic ceramic is their reputed magnetoelectric (ME) coupling, while a ferroic property is by and large improved by means of the conjugate field (magnetic fields alter magnetization, electric fields alter polarization, and likewise). A magnetic field can adjust the electric polarization and an electric field can adjust the magnetization in a multiferroic [2].

In the recent past, the utilization of ferroelectric materials to transfer light into mechanical, electrical, or chemical energy has enticed vast attention for understanding the mechanisms in addition to applications in photovoltaic, photocatalytic, and photo-transducer devices [3]-[9]. The huge prospects for applications emanated from their distinctive ferroelectric properties and the spontaneous electric polarization owing to the disruption of powerful inversion symmetry [10]. Ferroelectrics can furthermore serve as novel candidates for photocatalysis with comparable advantages and mechanisms. Several researchers have established that ferroelectric resources can perform improved photocatalysis than their counterparts. Among all the multiferroics, $BiFeO_3$ (BFO) is an extensively studied material owing to its ferroelectric and magnetic transition temperature well above room temperature (RT) [11] [12]. In the last few years, a huge struggle has been put to gain both durable ferroelectric (FE) and ferromagnetic (FM) polarizations. The stereo-chemically active $6s^2$ lone pair of Bi^{3+} is accountable for the ferroelectric process in BFO while the remnant moment from the canted Fe^{3+} spins' structure is accountable for the weak ferromagnetic property of BFO [13]. The interaction between fields of magnetic and electric occurs as a result of lattice distortion of BFO on the application of an electric or a magnetic field [14]. This puts forward novel paths to the recommendation and appliance of information storage, spintronics, sensors, etc. The foremost troubles of BFO and additional resources of this family are their huge leakage current density originating from charge defects, non-stoichiometry and impurity phases in BFO which creates it complicated to achieve a well-saturated ferroelectric hysteresis loop and small dielectric loss and hence obstructs its sensible applications [15] [16] [17]. In order to enhance the electrical properties of BFO, a number of research teams have tried to substitute with trivalent rare-earth ions such as La^{3+}, Er^{3+}, Dy^{3+}, Sm^{3+} and Tb^{3+} at the Bi site of BFO [13] [18] [19]. The substitution has emanated in the decrease of the leakage current as well as upgrading of ferroelectric properties of BFO reasonably. In addition, a few results confirmed that better ferroelectric parameters were strongly interconnected to the structural change resulting from rare earth doping [20] [21] [22]. Doping at Bi^{3+} site with rare earth and alkaline earth metal elements and doping at Fe^{3+} site with transi-

tion metal elements have been lately studied [23] [24] [25] [26] [27] and improved multiferroic properties have been reported. Li *et al.* studied the effect of La and Mn co-doping in BFO on structural and multiferroic properties of BFO [24]. The saturation magnetization and saturation polarization were found to be improved due to the co-doping. The effect of Nd and Mn co-doping on electrical and magnetic properties of BFO was investigated by Hu *et al.* [27]. The enhanced ferromagnetic property was attained owing to the structural transition from orthorhombic to tetragonal. The doping reduced the leakage current significantly and hence improved the ferroelectric property. In the present research, we would like to investigate the response of Gd^{3+} and Cu^{2+} doping at Bi and Fe site of BFO respectively to the structural and multiferroic properties of BFO.

2. Experimental

2.1. Sample Preparation

The multiferroic $Bi_{0.85}Gd_{0.15}Cu_xFe_{1-x}O_3$ (BGCFO) ceramics have been synthesized using conventional ceramic method. The various steps of the sample preparation method are shown in **Figure 1**. The high purity powers of Bi_2O_3 (99.9%), Gd_2O_3 (99.9%), CuO (99.9%) and Fe_2O_3 (99.9%) are utilized as basic material for producing BGCFO ceramics. At first, the required stoichiometric constituents are weighted and the weighted powders are blended thoroughly by grinding. Grinding is performed to decrease the particle size to the micro level to facilitate the solid-state reaction to occur by atomic diffusion. In this case, mortar and pestle are utilized for grinding. Samples have been grinded for 6 hours. In hand milling process, particle size is decreased due to the friction of the powder with the pestle. Finer particles can lessen the sintering temperature and time remarkably. The grinded powders are fired at 750˚C for 4 hours. For a better degree of uniformity, the fired powders were grinded again for 2 hours. Before making disk and toroid shaped samples 1 - 2 drops (depending on the amount of sample) of polyvinyl alcohol (PVA) are added as a binder. The disk and toroid shaped

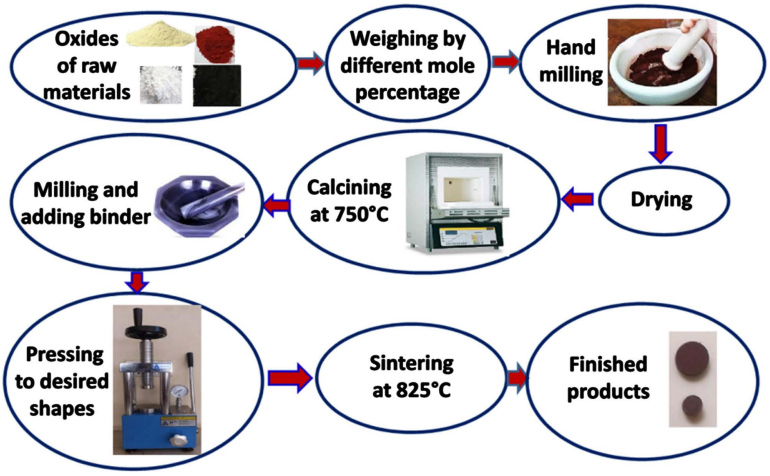

Figure 1. Various steps of conventional solid-state reaction method.

samples are made using a uniaxial hydraulic press with a pressure of 10 kN and 15 kN, respectively. These disk and toroid shaped samples are sintered at 825˚C for 4 hours with a heating rate of 10˚C per minute.

2.2. Characterization

X-ray diffraction is a non-catastrophic technique for detection and quantitative determination of different structural phases of any material. To investigate crystalline phases of the samples PHILIPS PW 3040 X'pert PRO X-ray diffractometer has been used. The samples are exposed to CuK_α radiation of wavelength, λ = 1.54178 Å with a primary beam of 40 kV and 30 mA with 0.02˚ sampling pitch and 1.0 second data collection step.

A 2θ scan is taken from 20˚ to 70˚ to obtain probable elementary peaks and Ni filter is applied to diminish CuK_α radiation.

The X-ray density ρ_x is measured applying the following expression:

$$\rho_x = \frac{nM}{N_A V}\,\mathrm{g/cm^3} \tag{1}$$

where, n is the number of atoms per unit cell, N_A is Avogadro's number (6.02×10^{23} mol^{-1}), M is the molecular weight, V is volume of the unit cell. The porosity is calculated from the equation

$$P(\%) = \frac{\rho_x - \rho_B}{\rho_x} \times 100\% \tag{2}$$

where, ρ_B is the bulk density which is measured by the formula:

$$\rho_B = \frac{m}{\pi r^2 t} \tag{3}$$

where m is the mass, r is the radius and t is the thickness of the pellet or ring [28].

Frequency dependent dielectric and magnetic characterization was performed at room temperature (RT) using WAYNE KERR Impedance Analyzer (Model No. 6500B). The real and imaginary part of complex initial permeability are calculated using the formulae:

$$\mu_i' = L_S / L_0 \tag{4}$$

$$\mu_i' = \mu_i'' \tan\delta \tag{5}$$

where L_S and L_0 are the self-inductances of the sample with and without the core L_0 is derived from the formula:

$$L_0 = \frac{\mu_0 N^2 S}{\pi \bar{d}} \tag{6}$$

Here N is the number of turns of the coil (N = 5), S is the cross-sectional area and $\bar{d} = (d_1 + d_2)/2$ is the average diameter, where d_1 and d_2 are the inner and outer diameter of the toroidal shaped sample, respectively [29]. With a Vibrating Sample Magnetometer (VSM) the magnetic characterization of BBFSO is made at a maximum applied field of ±1 T at RT. The pellets are painted for dielectric

measurements with conducting silver paste on both sides to confirm good electrical connection. The dielectric constant, ε', is computed using the relation:

$$\varepsilon' = \frac{Ct}{\varepsilon_0 A} \tag{7}$$

where C, A and ε_0 are the capacitance of the pellet, the cross-sectional area of the electrode and the permittivity of free space, respectively.

The ac conductivity of the samples is estimated with the formula:

$$\sigma_{ac} = \omega \varepsilon_0 \varepsilon' \tan\delta \tag{8}$$

where ω is the angular frequency and $\tan\delta$ is the dielectric loss. Real part (M') of dielectric modulus are computed applying the formulae:

$$M' = \frac{\varepsilon'}{\varepsilon'^2 + \varepsilon''^2} \tag{9}$$

3. Results and Discussion

3.1. Structural Characterization, Density and Porosity

The XRD patterns of BGCFO ceramics are illustrated in Figure 2(a). The peaks in the XRD patterns have been pointed out with their equivalent miller indices. The XRD patterns verified the synthesis of desired ceramics with few trace of impurity phases of $Bi_2Fe_4O_9$ and $Bi_{25}FeO_{40}$ [30] appeared for all the compositions. The undoped sample exhibits orthorhombic perovskite structure. A discontinuous series of structural changes with varying composition are observed for the doped samples as illustrated in Figure 2(b). The composition $x = 0.025$ exhibits rhombohedral structure and the other doped samples exhibit orthorhombic structure. The inconsistence structural change is due to the inhomogeneous diffusion of Cu in the lattice.

Figure 3 indicates the change of ρ_x, ρ_B and P as a function of composition sintered at 825˚C. The ρ_x is maximum for $x = 0.025$ which may be due to the structural transition. The ρ_B increases with Cu content reaches the highest at $x = 0.05$ and then reduces. The increase in ρ_B with Cu content is because of the fact that Cu stimulates grain development [31]. The decrease in ρ_B at higher

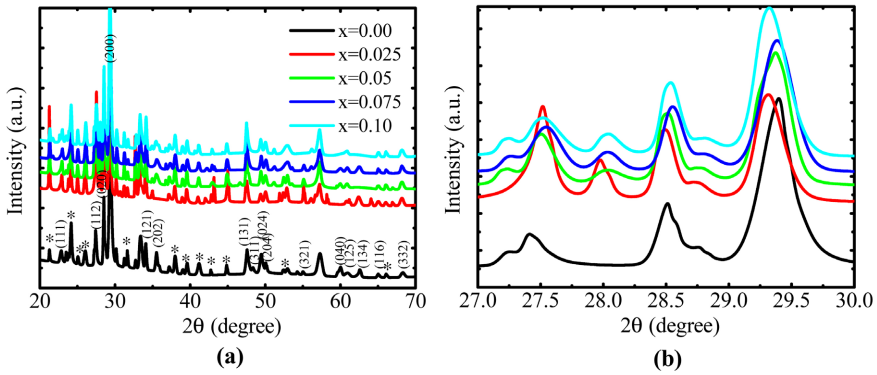

Figure 2. XRD patterns of BGCFO (a) in the range 20˚ - 70˚ (b) between 27˚ and 30˚.

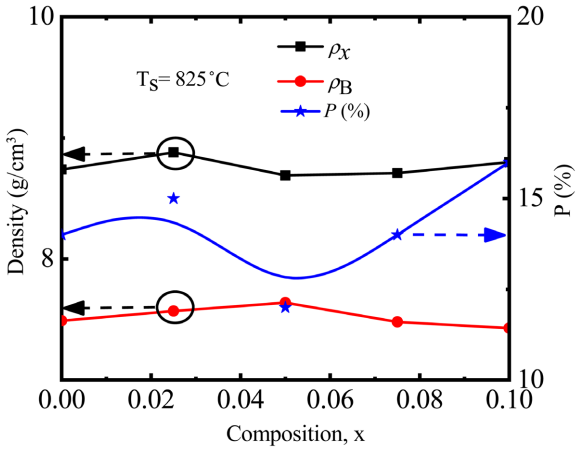

Figure 3. Variation of ρ_x, ρ_B and P of BGCFO as a function of composition.

Cu content may be due to the expanded intragranular porosity resulting from higher rate of grain growth. Porosity degrades the material quality and high value of porosity is undesirable. The lowest P is obtained for $x = 0.05$ composition.

3.2. Complex Initial Permeability

Permeability is one of the leading factors used in assessing magnetic materials. **Figure 4** indicates the change of μ_i' with frequency of BGCFO as a function of composition. The μ_i' persists quite steady over the whole frequency range for all the compositions. This is owing to the fact that their cut-off frequency falls outside the investigated frequency scale. The cut-off frequency is the frequency at which μ_i' gains 71% of its starting value. The above findings concurs well with the Globus model [32], which correlates the resonance frequency with permeability as given by $(\mu_i - 1)^{1/2} f_r = \text{constant}$. Conforming to this relationship, the higher the value of μ_i, the lower the value of f_r and vice-versa. The μ_i' goes up with Cu content up to $x = 0.5$ and then falls with additional rise in Cu content in the composition. The samples having maximum density show the highest μ_i' indicating a close relation between μ_i' and the density. The reduction of μ_i' at higher Cu concentration is because of the low density and defect of the samples resulting from the increased intragranular porosity.

Figure 5 indicates the change of $\tan\delta_M$ with frequency of BGCFO in the frequency range 100 kHz - 120 MHz. It is noticed from the figure that lowest $\tan\delta_M$ is obtained at higher frequency for all the compositions. The alteration of RQF in terms of frequency is revealed in **Figure 6**. For applied implementation the RQF is frequently taken as a measure of performance. It is detected that RQF rises with the frequency and tends to show a peak at high frequency. The highest RQF is attained for the sample with $x = 0.05$ for which the highest density is obtained.

3.3. Dielectric Property

Figure 7 illustrates the alteration of ε' with frequency of BGCFO in the

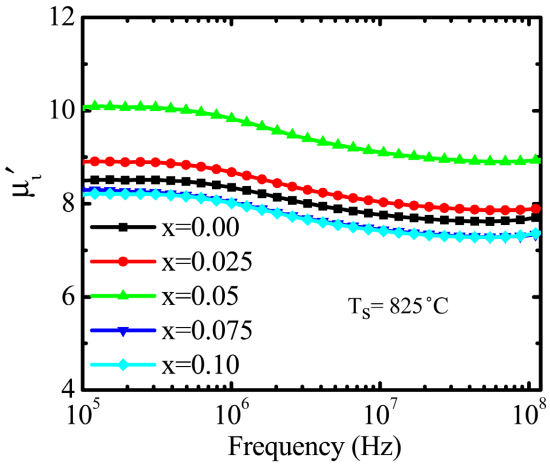

Figure 4. Variation of μ_i' as a function of frequency of BGCFO in the frequency range 100 kHz - 120 MHz.

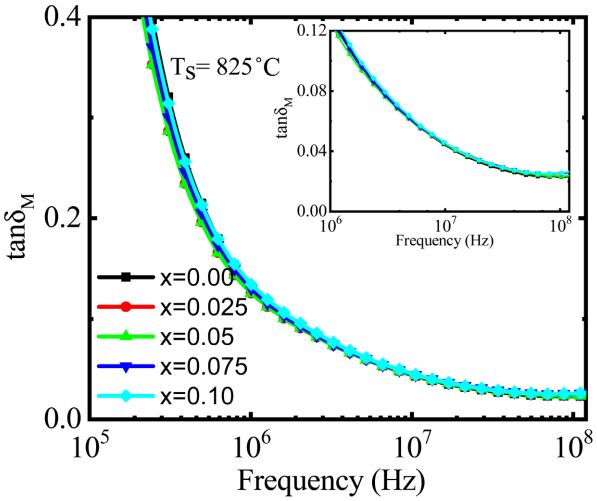

Figure 5. Variation of $\tan\delta_M$ as a function of frequency of BGCFO in the frequency range 100 kHz - 120 MHz.

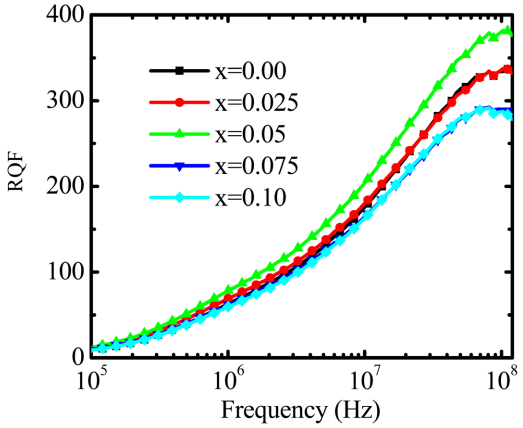

Figure 6. Variation of RQF as a function of frequency of BGCFO in the frequency range 100 kHz - 120 MHz.

frequency range 1 kHz - 10 MHz. It is perceived that ε' goes down with rising frequency up to 100 kHz. This dielectric dispersion at low-frequency is due to Maxwell-Wagner [33] [34] type interfacial polarization in agreement with Koop's phenomenological theory [35]. The interfacial polarization develops because of the heterogeneities of the sample following from porosity, interfacial defects and grain structure. These heterogeneities are produced in the sample during high temperature calcination and firing procedure. At higher frequencies, the ε' persists approximately frequency independent owing to the incapability of electric dipoles to go along the rapid change of the alternating applied electric field [36]. These frequency independent values are known as the static dielectric constant. The alteration of ε' with composition at 1 kHz frequency is indicated in **Figure 8**. The ε' first goes up with Cu content and then goes down. The maximum ε' is obtained for x = 0.025 composition. **Figure 9** demonstrates the change of $\tan\delta_E$ with frequency. The $\tan\delta_E$ is often ascribed to ion relocation, ion oscillation and distortion and electric polarization. Ion relocation is predominantly significant and strongly influenced by temperature and frequency. The losses owing to ion relocation rise at low-frequency and the temperature rises. The samples show low loss at high frequency because of the less mobility of charge carriers and might be useful for microwave applications.

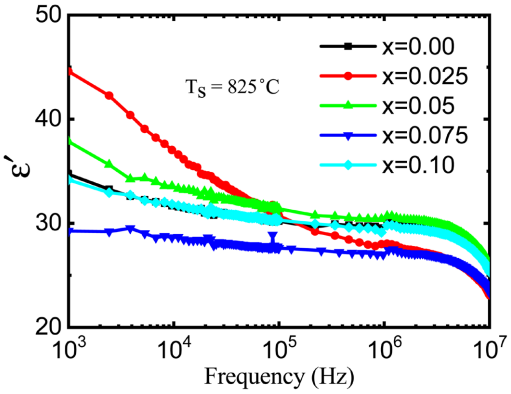

Figure 7. Variation of ε' with frequency of BGCFO in the frequency range 1 kHz - 10 MHz.

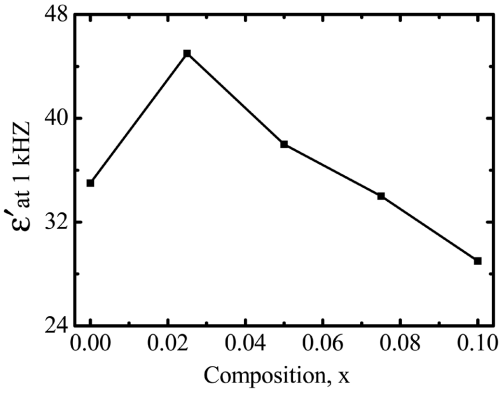

Figure 8. Variation of ε' with composition of BGCFO at 1 kHz frequency.

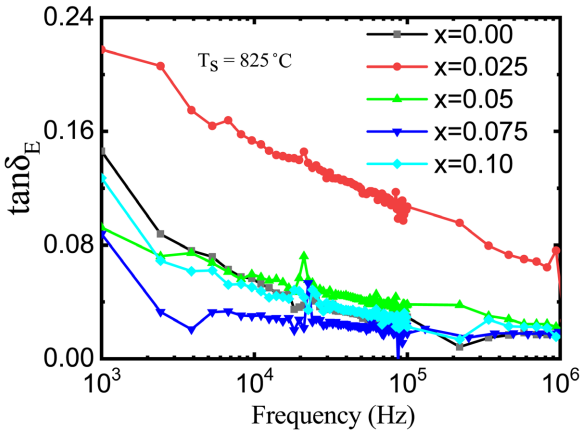

Figure 9. Variation of $\tan\delta_E$ with frequency of BGCFO in the frequency range 1 kHz - 10 MHz.

3.4. Complex Impedance Spectra Analysis

Figure 10 indicates the change of M' with frequency of the samples. The value of M' is low in the lower frequency part disclosing the relief of polaron hopping and minor function of electrode effect [37] [38]. The value of M' rises with frequency for all the samples and shows a sharp rise at high frequency. This is because of the incapability of several dipoles to follow up the rapid varying electric field at high frequency.

3.5. AC Conductivity

The σ_{AC} is an essential factor for interpretation the conduction process in different materials. **Figure 11** demonstrates the change of σ_{AC} with frequency at RT in the frequency range 1 kHz - 1 MHz. In lower part of the frequency, the conductivity is nearly frequency independent which resembles DC conductivity (σ_{DC}). The reason is that the resistive grain borders are more active at lower frequencies in agreement with the Maxwell–Wagner double layer model for dielectrics. However, in the higher frequency side (above 10 kHz) known as the hopping region, σ_{AC} rises [39] because at higher frequencies the conductive grains become more active thereby increasing hopping of charge carriers [40] and obeys the following Joncher's law: $\sigma_{AC}(\omega)=\sigma_0+A\omega^s$, where $\sigma_{AC}(\omega)$ is the total electrical conductivity, σ_0 is the frequency-independent dc conductivity, A is a temperature-dependent pre exponential factor known as the Universal Dynamic Response (UDR) [41] and s is the power law exponent which usually varies between 0 and 1 depending on the temperature. Alteration of $\log\sigma_{AC}$ in terms of $\log\omega$ is depicted in **Figure 12**. The $\log\sigma_{AC}$ rises almost linearly with $\log\omega$ for all the samples. The conduction mechanism in the low-frequency dispersive region mostly depends on the long-range hopping associated with grain boundaries [42] and that in the high frequency dispersive region is because of the restricted or reorientational short-range hopping inside the grain [42] [43].

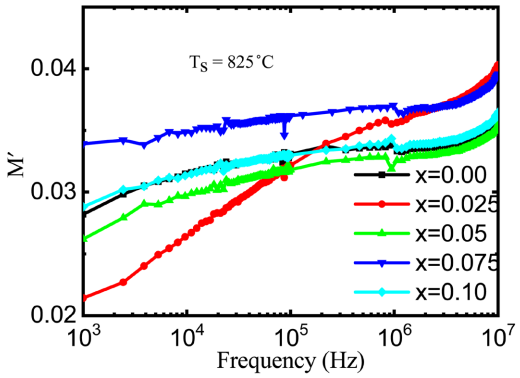

Figure 10. Real part (M') of electric modulus spectra of BGCFO in the frequency range 1 kHz - 10 MHz.

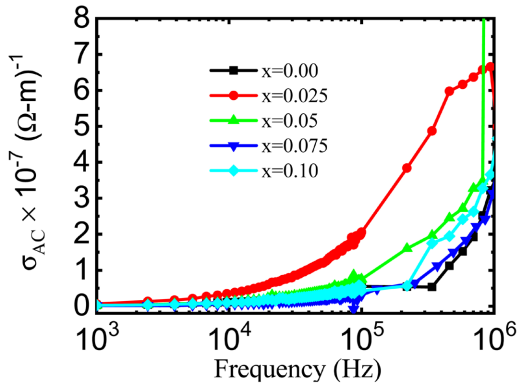

Figure 11. Variation of AC conductivity with frequency of BGCFO in the frequency range 1 kHz - 1 MHz.

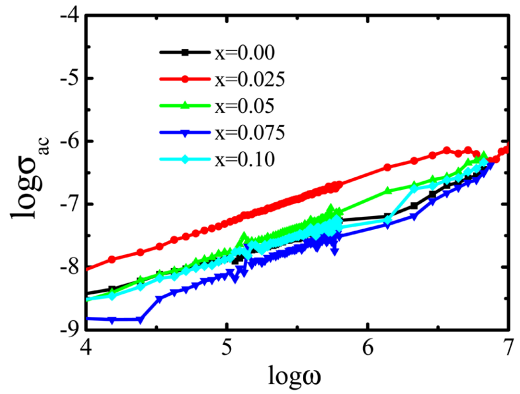

Figure 12. Variation of $\log\sigma_{AC}$ as a function of $\log\omega$ of BGCFO.

4. Conclusion

The multiferroic BGCFO ceramics are synthesized by a cost-effective solid-state reaction technique. The XRD patterns verify the synthesis of the desired structural phase with few traces of impurity phases of $Bi_2Fe_4O_9$ and $Bi_{25}FeO_{40}$. The composition x = 0.025 exhibits rhombohedral structure and the other doped samples exhibit orthorhombic structure. The ρ_x is maximum for x = 0.025,

which may be due to the structural transition. The ρ_B increases with Cu content reaches a maximum at $x = 0.05$ and then decreases. The μ_i' rises with Cu content up to $x = 0.5$ and then falls with an additional rise in Cu content in the composition. The samples having maximum ρ_B exhibit the highest μ_i' and RQF implying a direct relation of μ_i' and RQF with ρ_B. The dispersive character of ε' at lower frequencies is due to Maxwell-Wagner type interfacial polarization. At higher frequencies, the ε' persists nearly constant with frequency owing to the incapability of electric dipoles to follow up the rapid variation of the applied alternating electric field. The maximum ε' is obtained for $x = 0.025$ composition. The samples exhibit low loss at high frequency on account of the low mobility of charge carriers and can be used for microwave applications. In the low-frequency region, σ_{AC} remains almost constant but in the high frequency hopping region, σ_{AC} increases as the conductive grains are more active at high frequencies.

Acknowledgements

The authors greatly acknowledge Comilla University, Cumilla and University Grant Commission of Bangladesh for providing research grants for this work.

Conflicts of Interest

The authors declare no conflicts of interest regarding the publication of this paper.

References

[1] Schmid, H. (1994) Multi-Ferroic Magnetoelectrics. *Ferroelectrics*, **162**, 317-338. https://doi.org/10.1080/00150199408245120

[2] Spaldin, N.A., Cheong, S.W. and Ramesh, R. (2010) Multiferroics: Past, Present, and Future. *Physics Today*, **63**, 38. https://doi.org/10.1063/1.3502547

[3] Kundys, B., Viret, M., Colson, D. and Kundys, D.O. (2010) Light-Induced Size Changes in $BiFeO_3$ Crystals. *Nature Materials*, **9**, 803-805. https://doi.org/10.1038/nmat2807

[4] Lejman, M., *et al.* (2014) Giant Ultrafast Photo-Induced Shear Strain in Ferroelectric $BiFeO_3$. *Nature Communications*, **5**, 71-77. https://doi.org/10.1038/ncomms5301

[5] Yang, S.Y., *et al.* (2010) Above-Bandgap Voltages from Ferroelectric Photovoltaic Devices. *Nature Nanotechnology*, **5**, 143-147. https://doi.org/10.1038/nnano.2009.451

[6] Alexe, M. (2012) Local Mapping of Generation and Recombination Lifetime in $BiFeO_3$ Single Crystals by Scanning Probe Photoinduced Transient Spectroscopy. *Nano Letters*, **12**, 2193-2198. https://doi.org/10.1021/nl300618e

[7] Gao, F., *et al.* (2007) Visible-Light Photocatalytic Properties of Weak Magnetic $BiFeO_3$ Nanoparticles. *Advanced Materials*, **19**, 2889-2892. https://doi.org/10.1002/adma.200602377

[8] Deng, J., Banerjee, S., Mohapatra, S.K., Smith, Y.R. and Misra, M. (2011) Bismuth Iron Oxide Nanoparticles as Photocatalyst for Solar Hydrogen Generation from

Water. *Journal of Fundamentals of Renewable Energy and Applications*, **1**, 1-10. https://doi.org/10.4303/jfrea/R101204

[9] Kreisel, J., Alexe, M. and Thomas, P.A. (2012) A Photoferroelectric Material Is More than the Sum of Its Parts. *Nature Materials*, **11**, 260. https://doi.org/10.1038/nmat3282

[10] Young, S.M. and Rappe, A.M. (2012) First Principles Calculation of the Shift Current Photovoltaic Effect in Ferroelectrics. *Physical Review Letters*, **109**, Article ID: 116601. https://doi.org/10.1103/PhysRevLett.109.116601

[11] Catalan, G. and Scott, J.F. (2009) Physics and Applications of Bismuth Ferrite. *Advanced Materials*, **21**, 2463-2485. https://doi.org/10.1002/adma.200802849

[12] Eerenstein, W., Mathur, N.D. and Scott, J.F. (2006) Multiferroic and Magnetoelectric Materials. *Nature*, **442**, 759-765. https://doi.org/10.1038/nature05023

[13] Rai, R., Mishra, S.K., Singh, N.K., Sharma, S. and Kholkin, A.L. (2011) Preparation, Structures, and Multiferroic Properties of Single-Phase $BiRFeO_3$, R = la and Er Ceramics. *Current Applied Physics*, **11**, 508-512. https://doi.org/10.1016/j.cap.2010.09.003

[14] Fischer, P., Polomska, M., Sosnowska, I. and Szymanski, M. (1980) Temperature Dependence of the Crystal and Magnetic Structures of $BiFeO_3$. *Journal of Physics C*: *Solid State Physics*, **13**, 1931-1940. https://doi.org/10.1088/0022-3719/13/10/012

[15] Cheong, S.W. and Mostovoy, M. (2007) Multiferroics: A Magnetic Twist for Ferroelectricity. *Nature Materials*, **6**, 13-20. https://doi.org/10.1038/nmat1804

[16] Pradhan, A.K., *et al.* (2005) Magnetic and Electrical Properties of Single-Phase Multiferroic $BiFeO_3$. *Journal of Applied Physics*, **97**, Article ID: 093903. https://doi.org/10.1063/1.1881775

[17] Wang, Y.P., Zhou, L., Zhang, M.F., Chen, X.Y., Liu, J.M. and Liu, Z.G. (2004) Room-Temperature Saturated Ferroelectric Polarization in $BiFeO_3$ Ceramics Synthesized by Rapid Liquid Phase Sintering. *Applied Physics Letters*, **84**, 1731-1733. https://doi.org/10.1063/1.1667612

[18] Mahesh Kumar, M., Palkar, V.R., Srinivas, K. and Suryanarayana, S.V. (2000) Ferroelectricity in a Pure $BiFeO_3$ Ceramic. *Applied Physics Letters*, **76**, 2764-2766. https://doi.org/10.1063/1.126468

[19] Pattanayak, S., Choudhary, R.N.P., Das, P.R. and Shannigrahi, S.R. (2014) Effect of Dy-Substitution on Structural, Electrical and Magnetic Properties of Multiferroic $BiFeO_3$ Ceramics. *Ceramics International*, **40**, 7983-7991. https://doi.org/10.1016/j.ceramint.2013.12.148

[20] Dong, G., Tan, G., Luo, Y., Liu, W., Ren, H. and Xia, A. (2014) Investigation of Tb-Doping on Structural Transition and Multiferroic Properties of $BiFeO_3$ Thin Films. *Ceramics International*, **40**, 6413-6419. https://doi.org/10.1016/j.ceramint.2013.11.089

[21] Hu, G.D., Cheng, X., Wu, W.B. and Yang, C.H. (2007) Effects of Gd Substitution on Structure and Ferroelectric Properties of $BiFeO_3$ Thin Films Prepared Using Metal Organic Decomposition. *Applied Physics Letters*, **91**, Article ID: 232909. https://doi.org/10.1063/1.2822826

[22] Jiang, B., Li, X., Zhang, H., Sun, W., Liu, J. and Hu, G. (2012) Large and Stable Piezoelectric Response in $Bi_{0.97}Nd_{0.03}FeO_3$ Thin Film. *Applied Physics Letters*, **100**, Article ID: 172904. https://doi.org/10.1063/1.4705427

[23] Fujino, S., *et al.* (2008) Combinatorial Discovery of a Lead-Free Morphotropic Phase Boundary in a Thin-Film Piezoelectric Perovskite. *Applied Physics Letters*, **92**, Article ID: 202904. https://doi.org/10.1063/1.2931706

[24] Li, B., Wang, C., Liu, W., Ye, M. and Wang, N. (2013) Multiferroic Properties of La and Mn Co-Doped $BiFeO_3$ Nanofibers by Sol-Gel and Electrospinning Technique. *Materials Letters*, **90**, 45-48. https://doi.org/10.1016/j.matlet.2012.09.012

[25] Wang, Y. and Nan, C.W. (2006) Enhanced Ferroelectricity in Ti-Doped Multiferroic $BiFeO_3$ Thin Films. *Applied Physics Letters*, **89**, Article ID: 052903. https://doi.org/10.1063/1.2222242

[26] Li, J., Liu, K., Xu, J., Wang, L., Bian, L. and Xu, F. (2013) Structure-Dependent Electrical, Optical and Magnetic Properties of Mn-Doped $BiFeO_3$ Thin Films Prepared by the Sol-Gel Process. *Journal of Materials Science Research*, **2**, 75-81. https://doi.org/10.5539/jmsr.v2n3p75

[27] Hu, Z., *et al.* (2010) Effects of Nd and High-Valence Mn Co-Doping on the Electrical and Magnetic Properties of Multiferroic $BiFeO_3$ Ceramics. *Solid State Communications*, **150**, 1088-1091. https://doi.org/10.1016/j.ssc.2010.03.015

[28] Cullity, B.D. and Graham, C.D. (2008) Introduction to Magnetic Materials. Wiley, Hoboken. https://doi.org/10.1002/9780470386323

[29] Goldman, A. (1999) Handbook of Modern Ferromagnetic Materials. Springer, Berlin. https://doi.org/10.1007/978-1-4615-4917-8

[30] Priya, A.S., Banu, I.B.S. and Anwar, S. (2016) Influence of Dy and Cu Doping on the Room Temperature Multiferroic Properties of $BiFeO_3$. *Journal of Magnetism and Magnetic Materials*, **401**, 333-338. https://doi.org/10.1016/j.jmmm.2015.10.059

[31] Raghavan, C.M., Kim, J.W. and Kim, S.S. (2013) Structural and Ferroelectric Properties of Chemical Solution Deposited (Nd, Cu) Co-Doped $BiFeO_3$ Thin Film. *Ceramics International*, **39**, 3563-3568. https://doi.org/10.1016/j.ceramint.2012.10.182

[32] Globus, A. (1977) Magnetization Mechanismssome Physical Considerations about the Domain Wall Size Theory of Magnetization Mechanisms. *Le Journal de Physique Colloques*, **38**, C1-1-C1-15. https://doi.org/10.1051/jphyscol:1977101

[33] Maxwell, J.C. (2011) Electricity and Magnetism. In: Maxwell, J.C., Ed., *A Treatise on Electricity and Magnetism*, Cambridge University Press, Cambridge, 31-34. https://doi.org/10.1017/CBO9780511709333

[34] Wagner, K.W. (1913) Zur Theorie der unvollkommenen Dielektrika. *Annals of Physics*, **345**, 817-855. https://doi.org/10.1002/andp.19133450502

[35] Koops, C.G. (1951) On the Dispersion of Resistivity and Dielectric Constant of Some Semiconductors at Audio-Frequencies. *Physical Review*, **83**, 121-124. https://doi.org/10.1103/PhysRev.83.121

[36] Patankar, K.K., Dombale, P.D., Mathe, V.L., Patil, S.A. and Patil, R.N. (2001) AC Conductivity and Magnetoelectric Effect in $MnFe_{1.8}Cr_{0.2}O_4$-$BaTiO_3$ Composites. *Materials Science & Engineering B: Solid-State Materials for Advanced Technology*, **87**, 53-58. https://doi.org/10.1016/S0921-5107(01)00695-X

[37] Kaiser, M. (2012) Electrical Conductivity and Complex Electric Modulus of Titanium Doped Nickelzinc Ferrites. *Physica B: Condensed Matter*, **407**, 606-613. https://doi.org/10.1016/j.physb.2011.11.043

[38] Choudhary, R.N.P., Pradhan, D.K., Tirado, C.M., Bonilla, G.E. and Katiyar, R.S. (2007) Effect of La Substitution on Structural and Electrical Properties of $Ba(Fe_{2/3}W_{1/3})O_3$ Nanoceramics. *Journal of Materials Science*, **42**, 7423-7432. https://doi.org/10.1007/s10853-007-1835-z

[39] Bidault, O., Goux, P., Kchikech, M., Belkaoumi, M. and Maglione, M. (1994) Space-Charge Relaxation in Perovskites. *Physical Review B*, **49**, 7868-7873. https://doi.org/10.1103/PhysRevB.49.7868

[40] Verma, K., Kumar, A. and Varshney, D. (2012) Dielectric Relaxation Behavior of a $xCo_{1-x}Fe_2O_4$ (A = Zn, Mg) Mixed Ferrites. *Journal of Alloys and Compounds*, **526**, 91-97. https://doi.org/10.1016/j.jallcom.2012.02.089

[41] Jonscher, A.K. (1977) The "Universal" Dielectric Response. *Nature*, **267**, 673-679. https://doi.org/10.1038/267673a0

[42] Peláiz-Barranco, A., Gutiérrez-Amador, M.P., Huanosta, A. and Valenzuela, R. (1998) Phase Transitions in Ferrimagnetic and Ferroelectric Ceramics by Ac Measurements. *Applied Physics Letters*, **73**, 2039-2041. https://doi.org/10.1063/1.122360

[43] Funke, K. (1993) Jump Relaxation in Solid Electrolytes. *Progress in Solid State Chemistry*, **22**, 111-195. https://doi.org/10.1016/0079-6786(93)90002-9